BJ www.biochemj.org

BJ Structure

Biochem. J. (2008) **415**, 217–223 (Printed in Great Britain) doi:10.1042/BJ20081000

Structural and kinetic differences between human and *Aspergillus fumigatus* D-glucosamine-6-phosphate *N*-acetyltransferase

Ramon HURTADO-GUERRERO*, Olawale G. RAIMI*, Jinrong MIN†, Hong ZENG†, Laura VALLIUS*, Sharon SHEPHERD*, Adel F. M. IBRAHIM‡, Hong WU†, Alexander N. PLOTNIKOV†§[1] and Daan M. F. van AALTEN*[1]

*Division of Biological Chemistry and Drug Discovery, College of Life Sciences, University of Dundee, Dundee DD1 5EH, Scotland, U.K., †Structural Genomics Consortium, University of Toronto, 100 College Street, Toronto, Ontario, M5G 1L5, Canada, ‡Cloning Service, College of Life Sciences, University of Dundee, Dundee DD1 5EH, Scotland, U.K., and §Department of Physiology, University of Toronto, 112 College Street, Toronto, Ontario M5G 1L6, Canada

Aspergillus fumigatus is the causative agent of aspergillosis, a frequently invasive colonization of the lungs of immunocompromised patients. GNA1 (D-glucosamine-6-phosphate *N*-acetyltransferase) catalyses the acetylation of GlcN-6P (glucosamine-6-phosphate) to GlcNAc-6P (*N*-acetylglucosamine-6-phosphate), a key intermediate in the UDP-GlcNAc biosynthetic pathway. Gene disruption of *gna1* in yeast and *Candida albicans* has provided genetic validation of the enzyme as a potential target. An understanding of potential active site differences between the human and *A. fumigatus* enzymes is required to enable further work aimed at identifying selective inhibitors for the fungal enzyme. In the present study, we describe crystal structures of both human and *A. fumigatus* GNA1, as well as their kinetic characterization. The structures show significant differences in the sugar-binding site with, in particular, several non-conservative substitutions near the phosphate-binding pocket. Mutagenesis targeting these differences revealed drastic effects on steady-state kinetics, suggesting that the differences could be exploitable with small-molecule inhibitors.

Key words: *Aspergillus fumigatus*, inhibitor design, kinetics, mutagenesis, protein structure, UDP-GlcNAc biosynthesis, X-ray crystallography.

INTRODUCTION

Aspergillus fumigatus is a filamentous, cosmopolitan and ubiquitous saprophytic fungus [1]. Its natural ecological niche is soil, from which aerosols of conidia are released. If these reach the alveoli in the human lung, they may germinate and start an infection (colonization), leading to invasive or chronic aspergillosis, especially in immunocompromised patients. In these patients, the incidence of invasive infection can be as high as 50 %, with a 50 % mortality rate [2]. In the U.S.A., aspergillosis is the second most common opportunistic fungal infection in immunocompromised patients, accounting for as many as 20 % of fungal infections in patients who have received organ transplants [3]. Amphotericin B has long been the primary drug for the treatment of aspergillosis, although voriconazole has been described to represent an improvement against invasive aspergillosis [4], with itraconazole also providing some encouraging results [5]. Nevertheless, new drugs are urgently needed due to the inefficacy and side effects reported for amphotericin, itraconazole and voriconazole [6].

The fungal cell wall is essential for the viability of *Aspergillus fumigatus* and is mainly composed of a branched β(1,3)-glucan core bound to chitin, galactomannan and β(1,3-1,4)-glucan, embedded in an amorphous cement composed of α(1,3)-glucan, galactomannan and polygalactosamine [7]. Chitin is a β(1,4)-linked polymer of GlcNAc (*N*-acetylglucosamine), deposited by chitin synthase. Chitin, although a minor component of the *A. fumigatus* cell wall, is essential for cell viability and mother–daughter cell separation [8]. Chitin biosynthesis, which requires UDP-GlcNAc, is complex and involves several chitin synthases and ancillary proteins [8]. Normal levels of UDP-GlcNAc are required for chitin biosynthesis and subsequent cell wall assembly and growth [9]. UDP-GlcNAc is also a substrate for the synthesis of GPI (glycosylphosphatidylinositol) anchors of cell wall proteins [10] and the synthesis of N-linked and O-linked glycans.

The UDP-GlcNAc biosynthetic pathway is formed by four enzymes. The first enzyme, GFA1 (glutamine:fructose-6-phosphate amidotransferase), is bifunctional, converting fructose-6-phosphate and glutamine into GlcN-6P (glucosamine-6-phosphate) [11]. The second enzyme in the pathway is GNA1 (D-glucosamine-6-phosphate *N*-acetyltransferase), which converts AcCoA (acetyl-CoA) and GlcN-6P into CoA and GlcNAc-6P (*N*-acetylglucosamine-6-phosphate) [11]. The third enzyme, GlcNAc phosphomutase, converts GlcNAc-6P into GlcNAc-1P, employing glucose-1,6-bisphosphate as a co-factor [12]. The final enzyme, UDP-*N*-acetylglucosamine pyrophosphorylase, converts UTP and GlcNAc-1P into UDP-GlcNAc and pyrophosphate [11,13]. GNA1 belongs to the superfamily of GNATs (GCN5-related *N*-acetyltransferases), widely distributed in nature, which use acyl-CoAs to acylate their cognate substrates [14]. Examples of key members of this superfamily include: aminoglycoside, serotonin and glucosamine-6-phosphate *N*-acetyltransferases, histone acetyltransferase, mycothiol synthase, protein α-*N*-myristoyltransferase and the FEM family of acyltransferases [14]. More than 24 crystal structures of members of this superfamily have been solved, and, despite poor sequence conservation, they all have in common a structurally conserved α/β fold [14].

Abbreviations used: AcCoA, acetyl-CoA; GlcNAc, *N*-acetylglucosamine; GlcNAc-6P, *N*-acetylglucosamine-6-phosphate; GlcN-6P, glucosamine-6-phosphate; GNA1, D-glucosamine-6-phosphate *N*-acetyltransferase; *Af*GNA1, *Aspergillus fumigatus* GNA1; GNAT, GCN5-related *N*-acetyltransferase; GST, glutathione transferase; *Hs*GNA1, human GNA1; IPTG, isopropyl β-D-thiogalactoside; PEG, poly(ethylene glycol); RMSD, root mean square deviation; *Sc*GNA1, *Saccharomyces cerevisiae* GNA1; WT, wild-type.

[1]Correspondence can be addressed to either of these authors (email alexander.plotnikov@mssm.edu or dava@davapc1.bioch.dundee.ac.uk).

The co-ordinates and structure factors have been deposited in the PDB with the following entry codes: 2HUZ and 2O28 for apo-HsGNA1 and the HsGNA1–CoA–GlcNAc-6P complex respectively, and entry code 2VXK for the AfGNA1–CoA-GlcNAc-6P complex.

The key role that GNA1 plays in eukaryotes was first highlighted by a report of *Saccharomyces cerevisiae gna1* disruption, producing a lethal phenotype [15]. It was later reported that *Candida albicans* lacking *gna1* was viable only in medium containing high concentrations of *N*-acetylglucosamine, and showed significantly reduced virulence in a murine model of candidiasis [16]. Although this appears to genetically validate GNA1 as a potential antifungal drug target, it has also been described that the inactivation of the mouse *gna1* gene is lethal [17], reflecting the essential role of this enzyme in higher eukaryotes. Therefore it is imperative to identify structural differences between human and *A. fumigatus* GNA1 that would be exploitable for selective antifungal drug design. In the present study, we have investigated such potentially exploitable differences in the active sites of *Hs*GNA1 (human GNA1) and *Af*GNA1 (*A. fumigatus* GNA1) with the aim of providing further validation of GNA1 as a drug target for the treatment of aspergillosis. We present high-resolution crystal structures of *Af*GNA1 and *Hs*GNA1 in complex with products, and the kinetic characterization of these enzymes. By detailed comparison of the active sites of both enzymes, potentially exploitable differences are revealed and validated using site-directed mutagenesis.

MATERIALS AND METHODS

Cloning of *Af*GNA1 and *Hs*GNA1

The *A. fumigatus gna1* gene was obtained by PCR from genomic DNA using the forward primer 5′-GGATCCATGACCAACGCAACCATTGCTCCGAC-3′ and the reverse primer 5′-CTCGAGTCATCAGTAGTAGTGCGCCATCTCCAAC-3′ which contain BamHI and XhoI restriction sites. The PCR product was cloned into the pCR2.1 vector (Invitrogen) and subsequently digested with BamHI and XhoI and sub-cloned into the pGEX6P1 vector [which encodes a GST (glutathione transferase) tag and a PreScission protease cleavage site; Amersham Biosciences]. Site-directed mutants were generated following the QuikChange® protocol (Stratagene), using the KOD HotStart DNA polymerase (Novagene). All plasmids were verified by sequencing (College of Life sciences, University of Dundee, Dundee, Scotland, U.K.). DNA encoding full-length (amino acids 1–184) *Hs*GNA1 was amplified by PCR from the Mammalian Gene Collection clone (accession code gi:37620194) and subcloned into a modified pET28a-MHL vector (http://www.sgc.utoronto.ca/SGC-WebPages/toronto-vectors.php), downstream of the poly-histidine coding region.

Expression and purification

pGEX6P1-*Af*GNA1 was transformed into BL21 (DE3) pLysS and grown in LB (Luria–Bertani) medium with 50 μg/ml ampicillin. Cells were grown at 37 °C until reaching an optical density of 0.6 at 600 nm, after which the expression of the protein was induced with 0.25 mM IPTG (isopropyl β-D-thiogalactoside) at room temperature (23 °C) for an overnight incubation. The cells were harvested by centrifugation at 3480 ***g*** for 30 min and resuspended in a buffer [consisting of 25 mM Tris/HCl and 150 mM sodium chloride (pH 7.5)], containing a small spatula of lysozyme and DNAse, and one tablet of protease inhibitors cocktail (Calbiochem). The cells were disrupted by sonication and centrifuged at 19000 ***g*** at 4 °C for 30 min. The supernatant was incubated at 4 °C with glutathione–Sepharose 4B beads (Amersham Biosciences) previously equilibrated with the same buffer for 2 h and subsequently the GST was cleaved overnight with PreScission protease. The *Af*GNA1 protein was released from the beads and passed through a pre-equilibrated gel-filtration column as the last step of the purification. The protein was concentrated and analysed by SDS/PAGE. Purification yield was 3 mg of the protein per 1 litre of culture.

*Hs*GNA1 was expressed in *Escherichia coli* BL21 (DE3) codon plus RIL strain (Stratagene) in TB (Terrific Broth) in the presence of 50 μg/ml of kanamycin. Cells were grown at 37 °C to a *D* of 1.5 and induced by 1 mM IPTG and incubated overnight at 15 °C. Cells were harvested by centrifugation at 3480 ***g*** for 30 min at 4 °C. The cell pellets were frozen in liquid nitrogen and stored at − 80 °C. For the purification, the cell paste was thawed and resuspended in lysis buffer [50 mM Hepes/NaOH (pH 7.4), 500 mM NaCl, 5 mM imidazole, 2 mM 2-mercaptoethanol and 5 % (v/v) glycerol] with protease inhibitor (0.1 mM PMSF). The cells were lysed by passing through a microfluidizer (Microfluidics) at 20000 lbf/in^2 (1 lbf/in^2 = 6.9 kPa). The crude extract was cleared by centrifugation (19000 ***g*** for 30 min at 4 °C). The clarified lysate was loaded on to a 5 ml HiTrap chelating column (Amersham Biosciences), charged with Ni^{2+}. The column was washed with 10 column volumes of 20 mM Hepes/NaOH (pH 7.4), containing 500 mM NaCl, 50 mM imidazole and 5 % (v/v) glycerol, and the protein was eluted with elution buffer [20 mM Hepes/NaOH (pH 7.4), 500 mM NaCl, 250 mM imidazole and 5 % (v/v) glycerol]. The protein was dialysed against 20 mM Hepes/NaOH (pH 7.4), 500 mM NaCl and 5 % (v/v) glycerol in the presence of TEV (tobacco etch virus) protease. The dialysed protein was passed through a 5 ml Ni^{2+} HiTrap column and loaded on to a Superdex200 column (26 mm × 60 cm; Amersham Biosciences), equilibrated with 20 mM Pipes buffer and 250 mM NaCl (pH 6.5) at a flow rate of 4 ml/min. The pooled fractions containing *Hs*GNA1 were further purified to homogeneity by ion-exchange chromatography on a Source 30S column (10 mm × 10 cm; Amersham Biosciences), equilibrated with 20 mM Pipes (pH 6.5), and eluted with a linear gradient of NaCl up to a concentration of 500 mM (20 column volumes). The purification yield was 25 mg of the protein per 1 litre of culture.

Kinetics

Steady-state kinetics of WT (wild-type) and mutant enzymes were determined using a previous described protocol [18,19] with some modifications. AcCoA, GlcN-6P and CoA were supplied by Sigma. All measurements were performed in triplicate. Standard reactions consisted of 5 nM *Af*GNA1 (200 nM for the *Af*GNA1 mutants) or 20 nM *Hs*GNA1 in 25 mM Tris/HCl, 250 mM NaCl, 2 mM EDTA and 5 % (v/v) glycerol (pH 7.5) in a total volume of 50 μl, incubated at room temperature. The reactions were initiated by adding the protein and were stopped at different times depending on the enzyme with 50 μl of a solution containing 25 mM Bis-Tris-propane, 250 mM NaCl, 2 mM EDTA and 6.4 M guanidine chloride (pH 7.5). A 50 μl aliquot of DTNB [dithio-bis(2-nitrobenzoic acid)] solution (1 mM in 0.1 % DMSO) containing 25 mM Tris/HCl, 250 mM NaCl and 2 mM EDTA (pH 7.5) was added and the absorbance at 412 nm was determined. The absorbance was quantified using a Spectra max 340 PC (Molecular Devices). The absorbance intensity data were analysed with non-linear regression analysis using GRAFIT 5 [20], with the default equations for first-order reaction rates and Michaelis–Menten steady-state kinetics.

Crystallization, phasing and refinement

Two different crystal forms were obtained for *Af*GNA1. For the first crystal form, *Af*GNA1 at a concentration of 20 mg/ml was

Table 1 Details of data collection and structure refinement

Values between brackets are for the highest resolution shell. All measured data were included in structure refinement.

Data collection	*Af*GNA1 + lead	*Af*GNA1 + CoA + GlcNAc-6P	apo-*Hs*GNA1	*Hs*GNA1 + CoA + GlcNAc-6P
Space group	$P4_32_12$	$C222_1$	C2	$P2_1$
Unit cell (Å)	a = b = 54.36, c = 131.13	a = 70.60, b = 100.82, c = 55.35	a = 111.67, b = 47.65, c = 84.84, β = 123.52	a = 49.19, b = 63.76, c = 64.74, β = 91.81
Resolution range (Å)	20.00–1.80 (1.86–1.80)	20.0–1.80 (1.86–1.80)	70.71–2.67 (2.74–2.67)	45.41–1.80 (1.84–1.80)
Number of unique reflections	19096 (1839)	18376 (1790)	10659 (1058)	33633 (1834)
Redundancy	10.3 (11.0)	4.6 (4.6)	6.5 (6.6)	3.5 (2.0)
I/σI	10.5 (3.3)	21.2 (10.5)	8.3 (1.7)	10.5 (2.3)
Completeness (%)	99.9 (99.3)	98.2 (98.0)	98.8 (89.1)	89.6 (89.4)
R_{merge}	0.094 (0.616)	0.033 (0.150)	0.084 (0.432)	0.045 (0.216)
R, R_{free}		0.177, 0.215	0.205, 0.298	0.189, 0.237
RMSD from ideal geometry				
Bonds (Å)		0.015	0.011	0.012
Angles (°)		1.52	1.31	1.47
B-factor RMSD (Å^2)				
Backbone bonds		0.84	0.43	0.87
<B> (Å^2)				
Protein		18.8	29.3	27.1
CoA		19.1		29.1
GlcNAc-6P		27.4		30.1
Water		26.1	43.0	39.4

pre-incubated on ice for 10 min with 10 mM CoA and 30 mM GlcNAc-6P. The sitting-drop vapour-diffusion method was used to produce crystals by mixing 0.6 μl of the protein solution with an equal volume of mother liquor {100 mM Hepes, 200 mM $MgCl_2$, 22.5–30 % PEG [poly(ethylene glycol)] 3350 (pH 7.75)} at 20 °C. Bi-pyramidal crystals (space group $P4_32_12$) grew within 1 day. The second crystal form was obtained when *Af*GNA1 (17 mg/ml) was co-crystallized with 10 mM CoA and 10 mM GlcNAc-6P. Crystals were produced by mixing 0.6 μl of the protein–ligand solution with an equal volume of mother liquor (10–25 % PEG 1500; 2.5–15 % PEG 1000 and 7.5–22.5 % PEG 8000) at 20 °C. Bar-like shaped crystals (space group $C222_1$) grew within 3 days. The first crystal form was cryoprotected with 30 % PEG 3350 and the second crystal form was cryoprotected using 35 % PEG 1000 and 10 % PEG 8000 in the corresponding mother liquor, and frozen in a nitrogen gas stream cooled to 100 K. A SAD phasing strategy was employed on a $P4_32_12$ crystal soaked for 30 min in mother liquor containing 20 mM $PbCl_2$, using data collected at the European Synchrotron Radiation Facility (beamline BM14). Data were processed with the HKL suite [21]. Seven lead sites were located and refined with SHELX [22]. This resulted in phases to 2.2 Å (1 Å = 0.1 nm) with a figure of merit of 0.30, yielding a readily interpretable electron-density map. Phases were further improved by solvent-flattening, resulting in an electron density map that showed well-defined density for the protein, and was used for autotracing with warpNtrace [23], which built 143 out of 190 residues. The resulting model was improved by partial iterative refinement with REFMAC5 [24] interspersed with model building with COOT [25]. This partial model was then used to solve the structure of the $C222_1$ crystal form by molecular replacement with MOLREP [26] against 4 Å data (Table 1), giving a single solution (R-factor = 0.372) with one molecule in the asymmetric unit. Further refinement to 1.8 Å with REFMAC5 including TLS, interspersed with model building with COOT [25] yielded a model with the final statistics shown in Table 1. Models for ligands were not included until their conformations were well-defined by the unbiased $|F_o| - |F_c|$, φ_{calc} electron-density maps (Figure 4). Ligand topologies and co-ordinates were generated with PRODRG [27]. In the case of the CoA, the last seven atoms including the sulfhydryl group were not well-defined by the electron-density maps and were omitted from the model. WHAT IF [28] was used to check hydrogen bonds and PyMOL [29] was used to generate pictures.

Purified *Hs*GNA1 (16 mg/ml) was crystallized using the sitting-drop vapour-diffusion method by mixing 1 μl of protein solution with 1 μl of the reservoir solution containing 25 % PEG 4000, 0.2 M ammonium sulfate, 0.1 M sodium acetate, (pH 4.6) and 0.1 M yttrium chloride. For the ternary complex, purified *Hs*GNA1 protein was complexed with CoA and GlcNAc-6P (Sigma) at a 1:5:5 molar ratio of protein/CoA/GlcNAc-6P and crystallized using the hanging-drop vapour-diffusion method by mixing 2 μl of protein solution with 2 μl of the reservoir solution containing 27 % PEG 3350, 0.2 M $MgCl_2$ and 0.1 M bicine (pH 9.0). Crystals were soaked in the corresponding mother liquor supplemented with 20 % (v/v) glycerol as cryoprotectant before freezing in liquid nitrogen. X-ray diffraction data were collected at 100K at beamline 17ID of APS (Advanced Photon Source) at Argonne National Laboratory (Argonne, IL, U.S.A.). Data were processed using the HKL 2000 software package [21]. The structure of apo-*Hs*GNA1 was solved by molecular replacement using the program MOLREP [26] with the yeast GNA1 structure (PDB 1I1D [30]) as the search model and was partially refined. The partial model was then used as a molecular replacement search model against the ternary complex diffraction data. ARP/wARP was used for automatic model building [23] using the initial model phases. The graphics program COOT [25] was used for model building and visualization. Crystal diffraction data and refinement statistics are displayed in Table 1.

RESULTS AND DISCUSSION

Kinetics of *Af*GNA1 and *Hs*GNA1

*Af*GNA1 and *Hs*GNA1 were PCR-amplified and cloned into vectors suitable for overexpression in *E. coli* as GST-fusion and His-tagged proteins respectively. Purification using affinity,

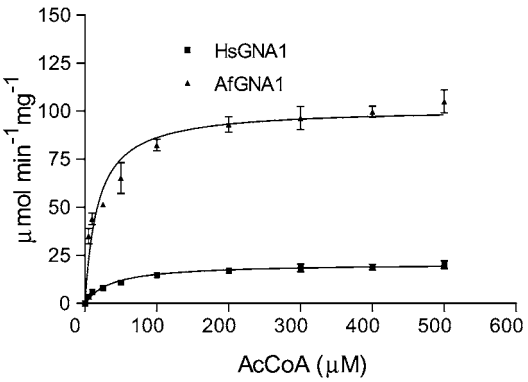

Figure 1 GNA1 kinetics

Initial steady-state velocities are shown for recombinant *Af*GNA1 and *Hs*GNA1 using different concentrations of AcCoA at a fixed (500 μM) concentration of GlcN-6P.

ion-exchange and size-exclusion chromatography yielded 4 mg and 25 mg of pure *Af*GNA1 and *Hs*GNA1 per litre of bacterial culture respectively.

*Af*GNA1 and *Hs*GNA1 steady-state kinetics were studied under linear conditions and with no more than 15 % of product formation. Both enzymes displayed classical Michaelis–Menten kinetics (Figure 1). *Af*GNA1 showed a K_m for AcCoA of 40 ± 6 μM, K_m for GlcN-6P of 71 ± 6 μM and k_{cat} of 38 ± 3 s^{-1} (the maximal specific activity was 107 $\mu mol \cdot min^{-1} \cdot mg^{-1}$ at pH 7.5). Under the same conditions *Hs*GNA1 showed a similar K_m for AcCoA and GlcN-6P, being 26 ± 3 μM and 97 ± 12 μM respectively. The k_{cat} of the human enzyme was 9 ± 0.2 s^{-1} (the specific activity was 25 $\mu mol \cdot min^{-1} \cdot mg^{-1}$). Overall, the fungal enzyme ($k_{cat}/K_m = 0.95$ $s^{-1} \cdot \mu M^{-1}$) was 3-fold more catalytically efficient for AcCoA than the human enzyme ($k_{cat}/K_m = 0.34$ $s^{-1} \cdot \mu M^{-1}$). The catalytic efficiency for GlcN-6P was 6-fold higher for *Af*GNA1 compared with *Hs*GNA1 ($k_{cat}/K_m = 0.53$ and 0.092 $s^{-1} \cdot \mu M^{-1}$ respectively). In terms of the maximal specific activity previously reported for GNA1 from various sources, the range is from 0.0054 to 12.2 $\mu mol \cdot min^{-1} \cdot mg^{-1}$, indicating that *Af*GNA1 would be one of the fastest GNA1s described so far (107 $\mu mol \cdot min^{-1} \cdot mg^{-1}$) [31,32].

*Af*GNA1 and *Hs*GNA1 adopt the GNAT fold

To understand the source of the kinetic differences observed between *Af*GNA1 and *Hs*GNA1 and to study potential amino acid differences in their active sites, the crystal structures of these enzymes were solved and refined against high-resolution synchrotron diffraction data. An apo-*Af*GNA1 structure was solved using a lead SAD experiment with a $P4_32_12$ crystal form (Table 1). A partially refined model from this was then used to solve a $C222_1$ crystal form of the *Af*GNA1 CoA–GlcNAc-6P complex by molecular replacement, subsequently refined to 1.80 Å resolution with an R-factor of 0.177 ($R_{free} = 0.215$; Table 1). An apo-*Hs*GNA1 structure was solved by molecular replacement with a C2 crystal form and partially refined. The resulting model was then used to solve a $P2_1$ crystal form of the *Hs*GNA1 CoA–GlcNAc-6P complex by molecular replacement followed by refinement to 1.8 Å resolution with an R-factor of 0.189 ($R_{free} = 0.237$; Table 1).

Both *Af*GNA1 and *Hs*GNA1 are homodimers in the crystal (and solution) and adopt essentially the same fold as the first GNA1 structure solved, that of *S. cerevisiae* (*Sc*GNA1) [30] (Figure 2A; 0.98 Å on 147 Cα atoms and 1.18 Å on 146 Cα atoms for *Af*GNA1 and *Hs*GNA1 superposed on the *Sc*GNA1 crystal structure respectively). Thus the typical signature of the GNAT superfamily is also present: an N-terminal strand (β1) followed by three α helices (α3-α4-α5), three antiparallel β strands, a signature central helix (α8), a fifth β strand, two α helices (α9 and α10) and a sixth and final β strand (Figure 2A). The only difference in secondary structure between the human and the fungal enzymes is that *Hs*GNA1 has a short additional β strand (β6, Figure 2A). A superposition of *Af*GNA1 and *Hs*GNA1 monomers gives an RMSD (root mean square deviation) of 1.3 Å on 159 Cα atoms, suggesting some conformational differences. Most of these differences are located to α1, α2, α5, α7, β2, β3 and β6, with α7 and β6 contributing residues to the substrate-binding site. Similarly, a sequence alignment between the two GNA1s shows that while these proteins share the four GNAT motifs (Figure 2B), the sequence identity is only 30 %. These significant structural and sequence differences prompted an investigation of whether such differences also extended to the active site.

*Af*GNA1 and *Hs*GNA1 possess different GlcN-6P subsites

A close inspection of the active sites of both enzymes showed that although the AcCoA-binding site is essentially conserved, significant differences are present in the GlcN-6P-binding site (Figures 3 and 4). The main differences are located to the residues contacting the α face of the sugar (Figures 3 and 4). These residues are, in *Af*GNA1, Val^{125}, Gly^{183}, Glu^{185} and Tyr^{189}, with the equivalent residues in *Hs*GNA1 being Arg^{116}, Glu^{175}, Tyr^{177} and Arg^{181} respectively. Arg^{116}, Glu^{175} and Arg^{181} of the human enzyme directly contact the sugar product, whereas Tyr^{177} lines a pocket just below it (Figure 4). Interestingly, the two arginine residues are substituted by smaller, neutral residues in the fungal enzyme, presumably with a reduced ability to interact with the phosphate on the sugar. Furthermore, the substitution of a glutamate residue (Glu^{175}) with a glycine (Gly^{183}) residue in the fungal enzyme generates a larger binding cavity. Thus the *Hs*GNA1 and *Af*GNA1 active sites show significant differences around the sugar-binding site.

Catalytic properties of *Af*GNA1–*Hs*GNA1 chimaeras

To study the contributions to substrate binding of the different residues lining the sugar-binding site, *Af*GNA1–*Hs*GNA1 chimaeras were constructed through site-directed mutagenesis, and their kinetic properties were studied (Table 2). Although all four mutant enzymes show effects in terms of reduced catalytic efficiency, this is, surprisingly, not only due to increases in K_m, but also decreases in k_{cat}. V125R and G183E show the largest effects on k_{cat}, with a 327-fold and 112-fold decrease respectively, compared with the *Af*GNA1 WT (Table 2). V125R also shows the largest effects on the K_ms for AcCoA and GlcN-6P, with a 5-fold and 8.5-fold decrease in the K_m of AcCoA and the K_m of GlcN-6P respectively. Apparently, the arginine residue present at this position in the human enzyme facilitates binding of the sugar substrate through interaction with the phosphate group (Figure 4). The precise positioning of the sugar could be important for the direct nucleophilic attack mechanism proposed previously [30], and this could explain the concomittant changes in k_{cat}. A similar explanation of effects on k_{cat} could be applied to the other three mutants which are likely to have effects on the precise position of the sugar in the binding site. Thus mutation of the four non-conserved residues lining the sugar-binding pocket suggests that they contributed to the kinetic differences between the *Af*GNA1 and *Hs*GNA1 enzymes.

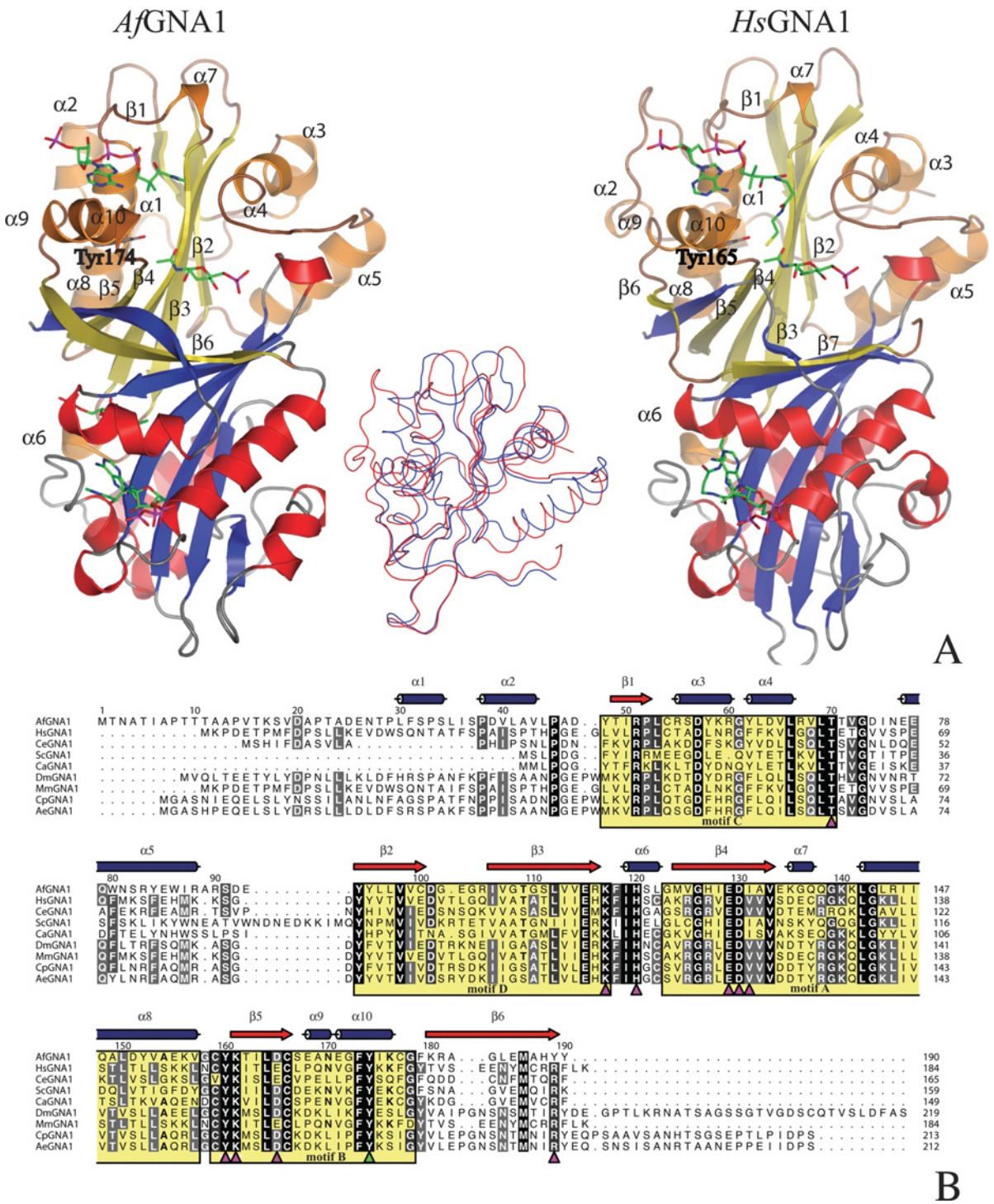

Figure 2 ***Af*GNA1 and *Hs*GNA1 fold and sequence conservation**

(**A**) Overall crystal structures of *Af*GNA1 and *Hs*GNA1. Secondary structure is shown in olive (strands) and brown (helices) for one monomer, and blue (helices) and red (strands) for the other monomer. A highly conserved active site tyrosine residue, that has been proposed to stabilize the leaving thiolate during catalysis [30], is shown as sticks in both crystal structures. CoA and GlcNAc-6P are shown as sticks with green carbon atoms. In the middle of this panel a superposition of the monomers from *Af*GNA1 (blue) and *Hs*GNA1 (red) are shown. (**B**) Multiple sequence alignment between *Af*GNA1, *Hs*GNA1, *Ce*GNA1 (*Caenorhabditis elegans* GNA1), *Sc*GNA1, *Ca*GNA1 (*C. albicans* GNA1), *Dm*GNA1 (*Drosophila melanogaster* GNA1), *Mm*GNA1 (*Mus musculus* GNA1), *Cp*GNA1 (*Culex pipiens* GNA1), *Ae*GNA1 (*Aedes aegypti* GNA1). Magenta triangles represent the residues from either *Af*GNA1 or *Hs*GNA1 involved in the binding of the sugar. The conserved tyrosine residue is shown as a green triangle. The four different motifs of the GNAT family are represented as yellow boxes.

Table 2 Comparison of the kinetic parameters between the human and the fungal enzyme and the corresponding mutations

K_m, k_{cat}, k_{cat}/K_m units are in μM, s^{-1} and $s^{-1} \cdot \mu M^{-1}$ respectively. All of the parameters were obtained at pH 7.5.

Enzyme form	K_m AcCoA	K_m GlcN-6P	k_{cat}	k_{cat}/K_m AcCoA	k_{cat}/K_m GlcN-6P
*Hs*GNA1	26 ± 3	97 ± 12	9 ± 0.2	0.34	0.092
*Af*GNA1	40 ± 6	71 ± 6	38 ± 3	0.95	0.53
*Af*GNA1-V125R	200 ± 40	600 ± 100	0.12 ± 0.01	0.00058	0.00019
*Af*GNA1-G183E	100 ± 18	56 ± 8	0.34 ± 0.017	0.0034	0.006
*Af*GNA1-E185Y	40 ± 7	30 ± 8	1.3 ± 0.07	0.031	0.042
*Af*GNA1-Y189R	86 ± 11	56 ± 8	1.7 ± 0.04	0.019	0.03

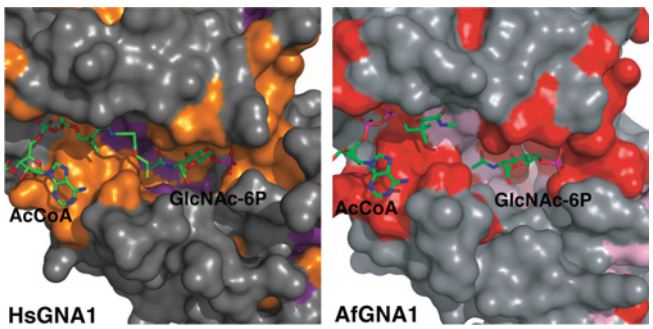

Figure 3 Conservation of the substrate-binding site

Molecular surfaces of *Hs*GNA1 and *Af*GNA1 are shown, coloured by sequence conservation. Orange/red, purple/pink and grey represent identity, conservative substitutions and non-conservative substitutions respectively. The ligands are represented as sticks with green carbon atoms.

Concluding remarks

There is sufficient data at the genetic level to suggest that GNA1 is an attractive antifungal drug target, provided two key issues can be addressed. First, although substrate-based inhibitors for the larger GNAT family, of which GNA1 is a member, have been reported, they do not possess drug-like properties and no significant *in vivo* effects of these molecules have been reported [33–35]. Secondly, the issue of selectivity requires careful consideration as a knockout of the mouse enzyme produced a lethal phenotype and GNA1 is generally believed to be essential in eukaryotes [17]. The latter issue was the focus of the present study, using *Af*GNA1 and *Hs*GNA1 as model enzymes. Kinetic analysis of these enzymes revealed differences in their Michaelis–Menten parameters. This was then corroborated by determination of their high-resolution crystal structures, which allowed a direct comparison between the active sites of these enzymes. Surprisingly, this revealed that structural differences between the two enzymes were mostly located to the sugar-binding site, whereas the AcCoA-binding site appeared to be more conserved. These changes affect not only the electrostatics, but also reveal a more spacious sugar-binding site in the *Af*GNA1 enzyme, whereas large side chains at these positions create a tighter pocket in the *Hs*GNA1 enzyme. Probing of these residues using mutagenesis suggests that they are important for sugar binding and positioning. Taken together these results may provide a useful framework for the discovery and/or design of molecules that show selective binding to *Af*GNA1 over *Hs*GNA1.

Although the work reported in the present study appears to provide data to support future drug discovery aimed at identifying *Af*GNA1 inhibitors, it has also uncovered a number of issues that may hamper such endeavours. While selective design of inhibitors may be achievable, such molecules may well possess undesirable properties. The substrate complexes described in the present study and published previously [30] show that interactions with the sugar are mostly of a polar nature, with almost no hydrophobic/

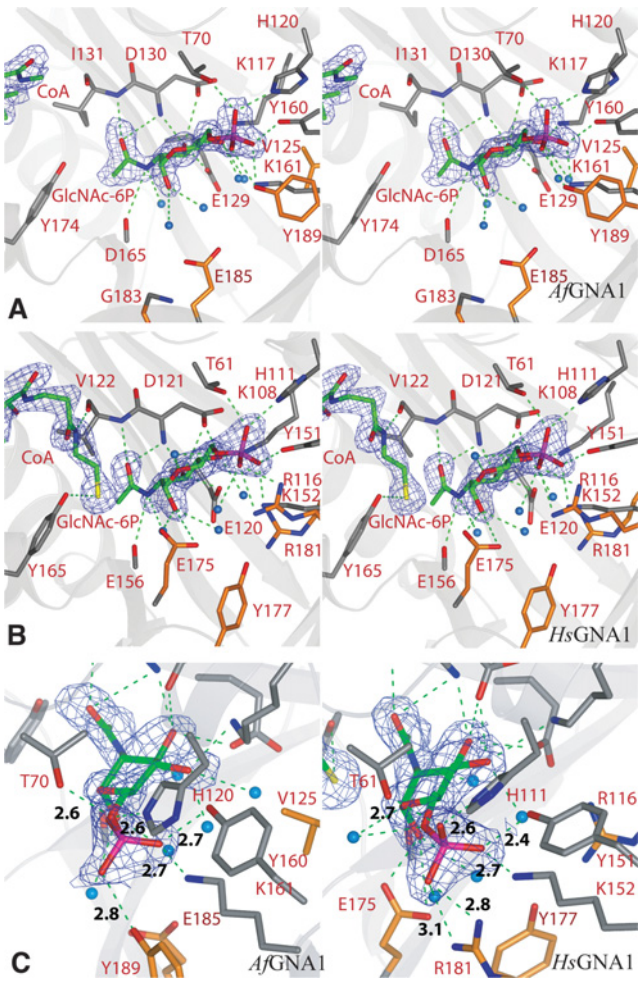

Figure 4 Comparison of the *Af*GNA1 and *Hs*GNA1 active sites

Stereo views of the structures of *Af*GNA1 (**A**) and *Hs*GNA1 (**B**) in complex with CoA and GlcNAc-6P, and detailed comparison of the phosphate-binding sites (**C**). The protein backbone is shown as a grey ribbon. Residues lining the active site are shown as sticks with grey carbon atoms (conserved residues) or orange carbon atoms (non-conserved residues). Ligands are shown as sticks with green carbon atoms. In the *Af*GNA1 structure, the terminal atoms of CoA, including the thiol, were omitted from the model due to a lack of electron density. Protein–ligand hydrogen bonds are shown as dotted green lines. Unbiased (i.e. before inclusion of any ligand model) (for *Af*GNA1) and a simulated annealing omit (for *Hs*GNA1) $|F_o| - |F_c|$, φ_{calc} electron-density maps are shown at 2.5 σ. Water molecules involved in hydrogen bonds with the ligand or the protein are shown as blue spheres. In (**C**), protein-phosphate distances (Å) are shown in black.

van der Waals interactions. Furthermore, if competition with both sugar and AcCoA (the latter also binding mainly through electrostatic interactions) is sought, the resulting molecules may be of a size beyond the spectrum normally associated with drug-likeness [36]. Indeed, the only well-characterized inhibitors known for the GNAT family of enzymes are truncated aminoglycoside-CoA bisubstrate analogues for aminoglycoside 6′-*N*-acetyltransferase [33], histone H3 peptides conjugated with CoA for GCN5 histone acetyltransferase [35] and the brominated CoA-*S*-acetyl-tryptamine bisubstrate analogue for serotonin *N*-acetyltransferase [34]. Nevertheless, the present study provides structural and kinetic data which may be useful tools in studies towards the discovery of novel GNA1 inhibitors.

We thank the European Synchrotron Radiation Facility, Grenoble, for the time at beamline BM14, and Lynsey McKenzie for experimental contributions. This work was supported by a Wellcome Trust Senior Research Fellowship and Project Grant, and the European Union FP6 STREP Fungwall programme to D.v.A. and by the Structural Genomics Consortium with funds from Genome Canada through the Ontario Genomics Institute, the Canadian Institutes for Health Research, the Canada Foundation for Innovation, the Ontario Challenge Fund, the Ontario Innovation Trust, the Wellcome Trust, GlaxoSmithKline, the Knut and Alice Wallenberg Foundation, and the Vinnova and Swedish Foundation for Strategic Research.

REFERENCES

1 Latge, J. P. (1999) *Aspergillus fumigatus* and aspergillosis. Clin. Microbiol. Rev. **12**, 310–350
2 Denning, D. W. (1998) Invasive aspergillosis. Clin. Infect. Dis. **26**, 781–803
3 Golan, Y. (2005) Overview of transplant mycology. Am. J. Health Syst. Pharm. **62**, S17–S21
4 Herbrecht, R., Denning, D. W., Patterson, T. F., Bennett, J. E., Greene, R. E., Oestmann, J.-W., Kern, W. V., Marr, K. A., Ribaud, P., Lortholary, O. et al. (2002) Voriconazole versus amphotericin b for primary therapy of invasive aspergillosis. N. Engl. J. Med. **347**, 408–415
5 Dupont, B. (1990) Itraconazole therapy in aspergillosis: study in 49 patients. J. Am. Acad. Dermatol. **23**, 607–614
6 Spanakis, E. K., Aperis, G. and Mylonakis, E. (2006) New agents for the treatment of fungal infections: clinical efficacy and gaps in coverage. Clin. Infect. Dis. **43**, 1060–1068
7 Fontaine, T., Mouyna, I., Hartland, R. P., Paris, S. and Latgé, J. P. (1997) From the surface to the inner layer of the fungal cell wall. Biochem. Soc. Trans. **25**, 194–199
8 Latgé, J. P., Mouyna, I., Tekaia, F., Beauvais, A., Debeaupuis, J. P. and Nierman, W. (2005) Specific molecular features in the organization and biosynthesis of the cell wall of *Aspergillus fumigatus*. Med. Mycol. **43**, S15–S22
9 Katz, D. and Rosenberger, R. F. (1970) A mutation in *Aspergillus nidulans* producing hyphal walls which lack chitin. Biochim. Biophys. Acta **208**, 452–460
10 Takeda, J. and Kinoshita, T. (1995) GPI-anchor biosynthesis. Trends Biochem. Sci. **20**, 367–371
11 Selitrennikoff, C. P. and Sonneborn, D. R. (1976) The last two pathway-specific enzyme activities of hexosamine biosynthesis are present in *Blastocladiella emersonii* zoospores prior to germination. Biochim. Biophys. Acta **451**, 408–416
12 Hofmann, M., Boles, E. and Zimmermann, F. K. (1994) Characterization of the essential yeast gene encoding *N*-acetylglucosamine-phosphate mutase. Eur. J. Biochem. **221**, 741–747
13 Etchebehere, L. C., Simon, M. N., Campanhã, R. B., Zapella, P. D., Véron, M. and Maia, J. C. (1993) Developmental regulation of hexosamine biosynthesis by protein phosphatases 2a and 2c in *Blastocladiella emersonii*. J. Bacteriol. **175**, 5022–5027
14 Vetting, M. W., S deCarvalho, L. P., Yu, M., Hegde, S. S., Magnet, S., Roderick, S. L. and Blanchard, J. S. (2005) Structure and functions of the GNAT superfamily of acetyltransferases. Arch. Biochem. Biophys. **433**, 212–226
15 Mio, T., Yamada-Okabe, T., Arisawa, M. and Yamada-Okabe, H. (1999) *Saccharomyces cerevisiae* gna1, an essential gene encoding a novel acetyltransferase involved in UDP-*N*-acetylglucosamine synthesis. J. Biol. Chem. **274**, 424–429
16 Mio, T., Kokado, M., Arisawa, M. and Yamada-Okabe, H. (2000) Reduced virulence of *Candida albicans* mutants lacking the gna1 gene encoding glucosamine-6-phosphate acetyltransferase. Microbiology **146**, 1753–1758
17 Boehmelt, G., Wakeham, A., Elia, A., Sasaki, T., Plyte, S., Potter, J., Yang, Y., Tsang, E., Ruland, J., Iscove, N. N. et al. (2000) Decreased UDP-GlcNAc levels abrogate proliferation control in emeg32-deficient cells. EMBO J. **19**, 5092–5104
18 Riddles, P., Blakeley, R. and Zerner, B. (1979) Ellman's reagent: 5,5′-dithiobis(2-nitrobenzoic acid)-a reexamination. Anal. Biochem. **97**, 75–81
19 Gehring, A. M., Lees, W. J., Mindiola, D. J., Walsh, C. T. and Brown, E. D. (1996) Acetyltransfer precedes uridylyltransfer in the formation of UDP-*N*-acetylglucosamine in separable active sites of the bifunctional glmu protein of *Escherichia coli*. Biochemistry **35**, 579–585
20 Leatherbarrow, R. J. (2001) GraFit Version 5, Erithacus Software Ltd., Horley, U.K.
21 Otwinowski, Z. and Minor, W. (1997) Processing of X-ray diffraction data collected in oscillation mode. Methods Enzymol. **276**, 307–326
22 Sheldrick, G. M. and Schneider, T. R. (1997) SHELXL: high-resolution refinement. Methods Enzymol. **277**, 319–343
23 Perrakis, A., Morris, R. and Lamzin, V. S. (1999) Automated protein model building combined with iterative structure refinement. Nat. Struct. Biol. **6**, 458–463
24 Murshudov, G. N., Vagin, A. A. and Dodson, E. J. (1997) Refinement of macromolecular structures by the maximum-likelihood method. Acta Crystallogr. Sect. D Biol. Crystallogr. **D53**, 240–255
25 Emsley, P. and Cowtan, K. (2004) Coot: model-building tools for molecular graphics. Acta Crystallogr. Sect. D Biol. Crystallogr. **D60**, 2126–2132
26 Vagin, A. and Teplyakov, A. (1997) Molrep: an automated program for molecular replacement. J. Appl. Crystallogr. **30**, 1022–1025
27 Schuettelkopf, A. W. and van Aalten, D. M. F. (2004) Prodrg: a tool for high-throughput crystallography of protein–ligand complexes. Acta Crystallogr. Sect. D Biol. Crystallogr. **D60**, 1355–1363
28 Vriend, G. (1990) WHAT IF: a molecular modeling and drug design program. J. Mol. Graph. **8**, 52–56
29 DeLano, W. L. (2004) Use of pymol as a communications tool for molecular science. Abstr. Pap. Am. Chem. Soc. **228**, 030-CHED
30 Peneff, C., Mengin-Lecreulx, D. and Bourne, Y. (2001) The crystal structures of apo and complexed *Saccharomyces cerevisiae* gna1 shed light on the catalytic mechanism of an amino-sugar *N*-acetyltransferase. J. Biol. Chem. **276**, 16328–16334
31 Pattabiraman, T. N. and Bachhawat, B. K. (1962) Purification of glucosamine-6-phosphate *N*-acetylase from sheep brain. Biochim. Biophys. Acta **59**, 681–689
32 Boehmelt, G., Fialka, I., Brothers, G., McGinley, M. D., Patterson, S. D., Mo, R., Hui, C. C., Chung, S., Huber, L. A., Mak, T. W. and Iscove, N. N. (2000) Cloning and characterization of the murine glucosamine-6-phosphate acetyltransferase emeg32. Differential expression and intracellular membrane association. J. Biol. Chem. **275**, 12821–12832
33 Gao, F., Yan, X., Shakya, T., Baettig, O. M., Ait-Mohand-Brunet, S., Berghuis, A. M., Wright, G. D. and Auclair, K. (2006) Synthesis and structure–activity relationships of truncated bisubstrate inhibitors of aminoglycoside 6′-*N*-acetyltransferases. J. Med. Chem. **49**, 5273–5281
34 Wolf, E., De Angelis, J., Khalil, E. M., Cole, P. A. and Burley, S. K. (2002) X-ray crystallographic studies of serotonin *N*-acetyltransferase catalysis and inhibition. J. Mol. Biol. **317**, 215–224
35 Poux, A. N., Cebrat, M., Kim, C. M., Cole, P. A. and Marmorstein, R. (2002) Structure of the GCN5 histone acetyltransferase bound to a bisubstrate inhibitor. Proc. Natl. Acad. Sci. U.S.A. **99**, 14065–14070
36 Lipinski, C. A. (2000) Drug-like properties and the causes of poor solubility and poor permeability. J. Pharmacol. Toxicol. Methods **44**, 235–249

Received 19 May 2008/27 June 2008; accepted 4 July 2008
Published as BJ Immediate Publication 4 July 2008, doi:10.1042/BJ20081000